Accuracy on Bovine Bone Fracture Detection of Two Dimensional B–Mode Ultrasound Images using Polynomial – Intensity Gradient

Rika Rokhana, Eko Mulyanto Yuniarno, I Ketut Eddy Purnama, Kayo Yoshimoto, Hideya Takahashi, Mauridhi Hery Purnomo

Abstract— **The detection of bone fracture uses X-rays or CT-scans device typically. These instruments have a negative effect of radiation and need high security for both patients and medical technicians. In this paper, we proposed a framework using the high–order polynomial approach and intensity gradient of two – dimensional B – mode ultrasound images for bone fracture detection. According to the ultrasound probe position, bone scanning process produce curved and flat contour surface. The local phase symmetry and morphology operation is used to extract the bone surface feature from the speckles and other noise. Then, a high order polynomial equation is used to obtain the center mass in the bone area. Two methods, Polynomial Tangent Perpendicular Line (PTPL) and Axis Perpendicular Line method are applied to determine the intensity gradient between adjacent columns based on the center of the mass bone area. These methods are tested to the bovine bone with no – fracture bone, and bone with transverse, oblique and comminuted fractures. Both PTPL and APL methods had 100% accuracy in the detection of fracture occurrence. For estimation width of fracture, the PTPL was more accurate than APL method. In the curved contour bone surface, the PTPL method has 1.14% error with the mean absolute error (MAE) of 0.016 mm. While the APL method has 2.63% error with the MAE of 0.04 mm. Meanwhile, in the flat contour bone surface, the PTPL method has 2.41% error with the MAE of 0.03 mm while the APL method has 3.21% error with the MAE of 0.04 mm.**

Index Terms—**bone fracture detection, intensity gradient, polynomial center of mass line, B – mode ultrasound image**

I. Introduction

BONE fracture is a medical condition where there are damages to the continuity of the bone, a crack or breaks reduces bone function [1]. A bone fracture may be the result of high – force impact or stress that the force exerted against a bone is stronger than the bone can structurally withstand, or a minimal trauma injury as a result of specific bone cancer, or osteogenesis imperfect [2][3].

The most common sites for bone fractures are on the long bones. Treatment includes immobilizing the bone with a plaster cast, or surgically inserting metal rods or plates to hold the bone pieces together [4][5]. Some complicated fractures may need surgery and surgical traction [6]. X – rays are commonly used in fracture checks to ensure proper medical action. These modalities provide high – quality visualization, especially on bone imaging [7]. Some studies have used X – rays modality to detect femur fractures based on texture analysis and superimpose the target border and covering the extracted skeleton [8][9].

For some cases requiring bone examination in three – dimensional (3D), a CT – scans is a useful device [10][11]. However, the CT – scans is expensive and rarely available in most hospitals, especially in undeveloped countries. Additionally, the X – rays and CT – scans have a radiation and ionization hazard in their operation, which require high security for both the patients and the medical technicians [12]. We can use the ultrasound (US) modality which have no ionizing radiation as an alternative method of orthopedics and related medical field. The other advantages of US – imaging compared to X – rays and CT – scans is it has lower cost, does not need special requirements to operate and it is a non – invasive method, therefore it is not painful to the patients. Some researchers have used ultrasonic modality to detect the occurrence of fractures [13][14][15][16].

The B – mode US image is obtained from US signals that were reflected by the object and visualized in 2D – image [17]. The pixel intensity is proportional to the amplitude of the reflective signal, which was affected by the direction of the reflected signal and the angle between the emitted and reflected signals [18]. This characteristic raises various noises in the US image and results in low image quality [19][20]. Speckles fulfilled almost all area in the US images. In the US bone imaging, the speckles and reverberations make it exceedingly difficult to determine the bone surface conditions accurately [21][22].

II. Data Aquisition and Proposed Method

A. Data Aquisition

Experiments held using ultrasound probe type L15 - 7 L40H US - 5, with Telemed Ultrasound – OEM Electronics system

Manuscript submitted November, 2018; accepted March, 2019. This work was supported by 2018-Improving the Quality of Intl.Publication Program from Directorate of Research, Technology and Higher Education and Intl. Publication Acceleration Program – ITS, Indonesia.

R. Rokhana, E.M. Yuniarno, I.K.E. Purnama, and M.H. Purnomo are with the Department of Electrical Engineering, Institut Teknologi Sepuluh Nopember, Surabaya, Indonesia (e-mail: rika16@mhs., ekomulyanto@, ketut@, hery@{ee.its.ac.id}).

E.M. Yuniarno, I.K.E. Purnama, and M.H. Purnomo are also with the Department of Computer Engineering, Institut Teknologi Sepuluh Nopember, Surabaya, Indonesia.

R. Rokhana is also with the Department of Electrical Engineering, Politeknik Elektronika Negeri Surabaya, Indonesia (e-mail: rika@pens.ac.id).

K. Yoshimoto and H. Takahashi are with the Graduate School of Engineering, Osaka City University, Osaka, Japan (e-mail: yoshimoto@, hideya@{elec.eng.osaka-cu.ac.jp}).

and Echo Wave II 3.5.0 software to activate the US scanning process and display the result in two – dimensional (2D) B – mode images. Fig. 1 illustrates the bone and US probe in the scanning process. The bone and head of the probe are immersed in water to ensure the US signal works. The probe is perpendicular to the bone, which the probe head is at the transverse or parallel position to the bone length direction, as shown in Fig. 2.

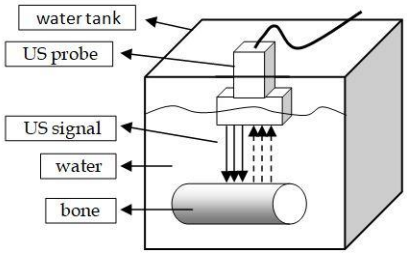

Fig. 1. US probe scanning to the bone surface. Both probe and bone are immersed in the water.

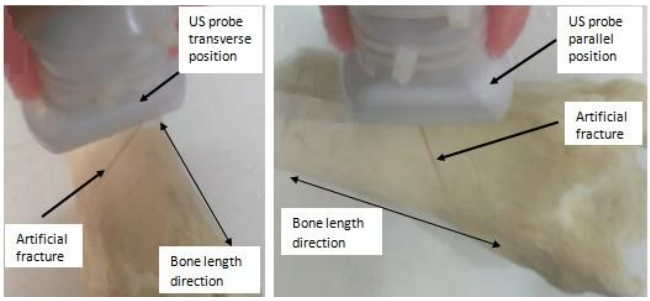

(a) (b)

Fig. 2. Probe position to the bone length direction: (a) in the transverse position and (b) in the parallel position.

The experiment uses the bovine's long bone (such as femur, tibia, metatarsal, etc.) with various diaphysis size in the no fracture bone and in the transverse and oblique fractures. Some samples use comminuted fractures. All fracture is created artificially by cutting part of the bone diaphysis manually with 1 – mm width. Transverse fractures are made transversally to the bone length direction, while the artificial oblique fracture pattern is formed at a 45° angle to the bone length, as shown in Fig. 3. Especially for comminuted fracture, we could not create a 1 – mm fracture width. In this experiment, the comminuted fracture was made by applying high impact pressure on the bone structure resulting in two or more irregular fractions. As a reference, manual measurement of the fracture width is done using a caliper.

In the US scanning process, the probe position is always at the shortest width of the fracture, in the parallel or transverse position to the bone length. When scanning of transverse fractured bone, probe position is parallel to the bone length, therefore the measured fracture width should be 1 – mm. On the oblique fracture bone scanning, the probe position could be in the transverse or parallel to the bone length. Using geometric calculation, the measured fracture width should be 1.414 mm (equal to $2r$, as shown in Fig. 3). Every sample bones produced 100 images for no fracture and 100 images for each transverse and oblique fracture. Except for costa bone image, the US image of all tested bone at the transverse probe position have curved surface contour. While the parallel probe position produced the flat surface contour. The costa bone image with transverse probe position is included in flat surface contour.

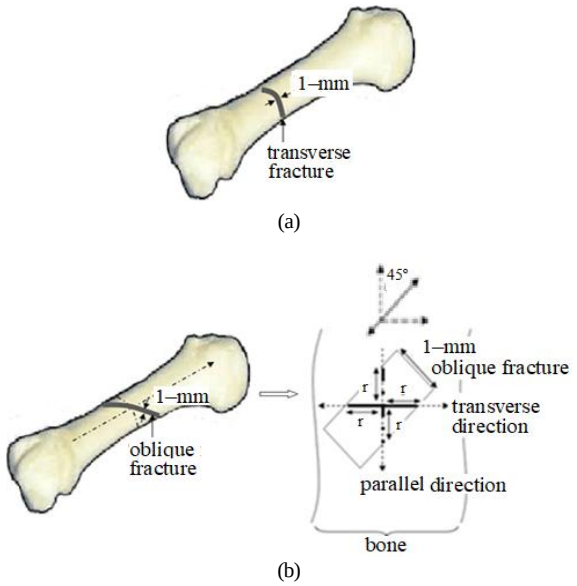

Fig. 3. (a) Transverse fracture (b) oblique fracture with 1.414 mm ($2r$) width.

B. Proposed Method

The basic idea of this study is detecting the bone fracture by calculating the intensity difference on adjacent pixels. In the B – mode US bone image, the bone area looks brighter than the surrounding areas. The no – fracture bone surface reflects all the US signals it received and depicted it in high – intensity pixels, close to white color. However, in the fractured bone, the hard surface of the bone is broken, and the US signal will be reflected by the spongy bone structure with lower reflective capability. Therefore, the pixels represented fracture has a lower intensity than pixels of no – fracture bone.

The first to do is to clean the bone image from noise to obtain bone area clearly and determine the center mass of bone area using high level polynomial approach. A set of the center of the mass form a polynomial center mass (PCM) line. Then we grouped the bone area in columns. A column is a straight line which passes the pixel on the polynomial center mass (PCM) line and connects the pixel on the upper boundary to the pixel on the lower limit of the bone area. The next step is to obtain the total intensity on each column and calculate the gradient intensity between adjacent column.

We propose two methods for calculating the total intensity each column, the Polynomial Tangent Perpendicular Line (PTPL) method and Axis Perpendicular Line (APL) method. The standard deviation and direction of the gradient intensity are used to determine the occurrence of fracture in the long bone.

1) Despeckling noise

The B – mode US images fulfill with speckles noise, making it difficult to determine the boundary between two adjacent tissues. Researchers have used many different filtering algorithms to improve the image quality [23][24][25][26][27][28]. This research used the local phase symmetry method [29][30][31][32] and combined with opening morphology operation to extract the bone feature. Fig. 4 shows 2D B – mode US grayscale – image of a bovine's costa bone. The white area indicated bone's area

which has unclear borders and causing an error in the bone fracture detection. If $I(x,y)$ denote the intensity pixels of grayscale ultrasound image, W_n^e and W_n^o denote the even – symmetric and odd – symmetric wavelets at scale n, then the response vector will be

$$[e_n(x,y), o_n(x,y)] = [I(x,y) * W_n^e, I(x,y) * W_n^o] \quad (1)$$

where $[e_n(x,y), o_n(x,y)]$ are the real and imaginary value of filter response, with the amplitude, $A_n(x,y)$, is $\sqrt{e_n(x,y)^2 + o_n(x,y)^2}$ and the phase, $\Phi_n(x,y)$, is $atan2(e_n(x,y), o_n(x,y))$.

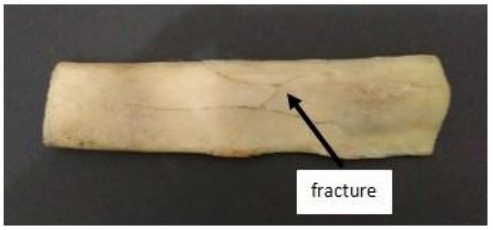

(a)

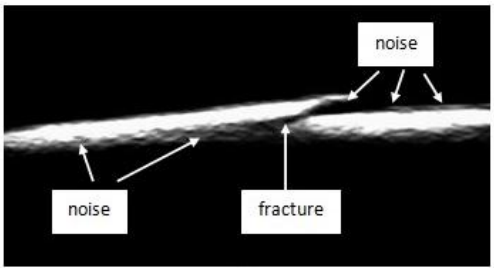

(b)

Fig. 4. (a) Costa bovine bone as the fracture model (b) 2D B – mode US bone image.

A weighted average is used to combine multiple scales filter response. The sum of these weighted differences produced phase symmetry. If ε is small value constant and T is noise compensation value, the normalized of phase symmetry, $Sym(x,y)$, is given by (2).

$$Sym(x,y) = \frac{\sum_n \left[|e_n(x,y)| - |o_n(x,y)| \right] - T}{\varepsilon + \sum_n A_n(x,y)} \quad (2)$$

Calculation of (2) produces a value between 0 and 1, where 1 indicating very significant feature, while 0 indicating no significance feature. The bright area in the ultrasound image produces high phase symmetry (close to 1). We used the $Sym(x,y)$ value of bone feature as threshold for transforming the 2D grayscale image, $I(x,y)$, into a black – white image, $J(x,y)$, given by (3).

$$J(x,y) = \begin{cases} 1, & if\ I(x,y) \geq t \\ 0, & otherwise \end{cases} \quad (3)$$

The area with high probability as a bone has a norm value above the threshold and will be represented in the white pixels, whereas other regions are black, as background. Fig. 5(a) shown the result. A narrow white area is often found around the true bone's areas. Although its intensity meets the requirement of bone, however, these small areas do not include bone's area. The pixels intensity in these narrow areas interferes with the process of identifying bone fracture. Therefore, these areas must be excluded. The morphology opening method is used to eliminate narrow noise area without changing the shape and size of the bone's area [33][34]. The image erosion, $G \ominus H$, followed by a dilation process, $G \oplus H$, will erase and then dilate the images G using the structuring element H, as shown in Fig. 5(b).

$$A \circ B = ((A \ominus B) \oplus B \quad (4)$$

$$A \ominus B = \{z \mid B_z \subseteq A\} \quad (5)$$

$$A \oplus B = \{ z \mid (B_z \cap A) \subseteq A \quad (6)$$

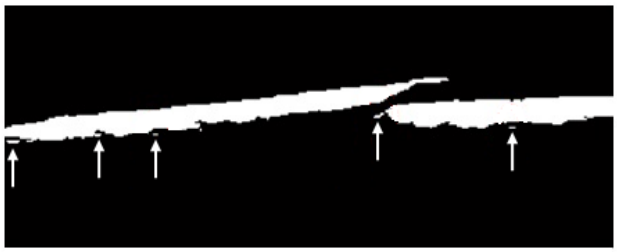

(a)

(b)

Fig. 5. (a) There are several narrow areas with the pixel's intensity such as intensity of bone pixels, but they are not bone pixels (b) image after denoising process.

2) Polynomial center of mass

US – bone is the 2D image in the (x,y) coordinate, where the x – axis is used as a reference to determination of the area of each column based on its mass center. Let $(\overline{x_i}, \overline{y_i})$ denote the mass center coordinate in the i^{th} column, where $\overline{x_i}$ is $1, 2, 3, \ldots, M$ and M is the number of columns in the bone areas, then the value of $\overline{y_i}$ given by (7).

$$\overline{y_i} = \left(\frac{1}{J_{tot}(x_i, y_i)}\right) \sum_{l=1}^{L} J(x_{il}, y_{il}) y_{il} \quad (7)$$

Where i refers to column number and $l = 1, 2, 3, \ldots, L$ represent the sequence of rows in the i^{th} column with L is the number of rows in the US image. $J(x_{il}, y_{il})$ is normalized intensity of pixels (x_{il}, y_{il}), whereas $J_{tot}(x_i, y_i) = \sum_{l=1}^{L} J(x_{il}, y_{il})$ is the total of normalized intensity in i^{th} column. A comprehensive calculation result a set of center mass positions $(\overline{x_1}, \overline{y_1}), (\overline{x_2}, \overline{y_2}), \ldots, (\overline{x_M}, \overline{y_M})$.

According to [35], the bone surface area is an area composed of several pixels which have saturated intensity. A proper mass center coordinates of the i^{th} column in the saturated image area, (x_i, y_i), could be obtained using a high order polynomial approach, given by (8).

$$y_i = \sum_{n=0}^{N} p_n \, {x_i}^n \quad (8)$$

Where p is polynomial coefficients, $n = 0, 1, 2, 3, \dots, N$ with N is the order of polynomial. Let denote $x_i = 1, 2, 3, \dots, M$, then the set of bone center mass coordinate generated by polynomial approach, $P = \{(x_1, y_1), (x_2, y_2), \dots, (x_M, y_M)\}$, is given by (9).

And, to fit mass center pixels in a smooth curve, it needs minimizing of Least Square Error (LSE) between (7) and (8) for each column, given by (10). The curve generated by center mass fitting is marked as Polynomial Center Mass (PCM) line, as shown in Fig. 6.

$$\begin{bmatrix} y_1 \\ y_2 \\ y_3 \\ \dots \\ y_M \end{bmatrix} = \begin{bmatrix} x_1^0 & x_1^1 & x_1^2 & \dots & x_1^n \\ x_2^0 & x_2^1 & x_2^2 & \dots & x_2^n \\ x_3^0 & x_3^1 & x_3^2 & \dots & x_3^n \\ \dots & \dots & \dots & \dots & \dots \\ x_M^0 & x_M^1 & x_M^2 & \dots & x_M^n \end{bmatrix} \begin{bmatrix} p_0 \\ p_1 \\ p_2 \\ \dots \\ p_n \end{bmatrix} \tag{9}$$

As a reference to total intensity calculation on each column, PCM line start from column position of image $i = 1$ until the end of the column, M, in the bone area. Let PCM_{fitt} is the proper ordinate of mass center on each column in the saturated bone area, then

$$PCM_{fitt} = min \sum_{i=1}^{M} \left(\overline{y_i} - \left(\sum_{n=0}^{n} p_n \, {x_i}^n \right) \right)^2 \tag{10}$$

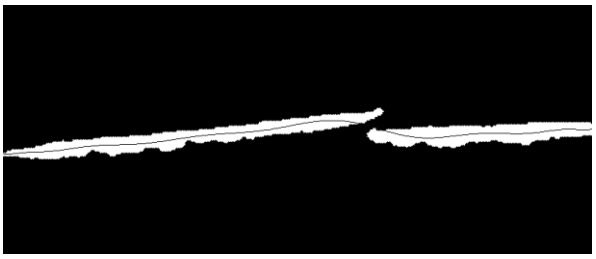

Fig. 6. Polynomial Center Mass (PCM) line

3) Total intensity

The total intensity calculation of each column requires a definite column boundary. In this experiment, the boundary area is the outermost edge of the bone area. Therefore, an upper boundary and a lower boundary is obtained by scanning pointing up or down from the point on the PCM line to the black – white image boundaries. If the intensity at a pixel (x, y) is 1 (means white), this pixel includes in the bone area. And, if the intensity of the pixel above it with coordinate $(x, y-1)$, or the pixel below it with coordinate $(x, y+1)$, is 0 (means black or background), this pixel is not bone area. In that case, the pixel (x, y) is marked and stored as the top or lowest edge, as shown in Fig. 7.

The pixel in the upper boundary noted as (x_{ui}, y_{ui}), and the pixel in the lower border, indicated as (x_{li}, y_{li}). The straight line $g(x_i)$ will connect pixels on the upper and lower boundary, and the total intensity is obtained by calculating the total intensity of pixels along the $g(x_i)$ line.

According to the above paragraph, we propose two methods to determine the straight lines that indicate the segment of each column: (*i*) straight line perpendicular to the tangent line of PCM line of each column or Polynomial Tangent Perpendicular Line (PTPL) method, (*ii*) straight line perpendicular to the x – axis of image area or Axis Perpendicular Line (APL) method.

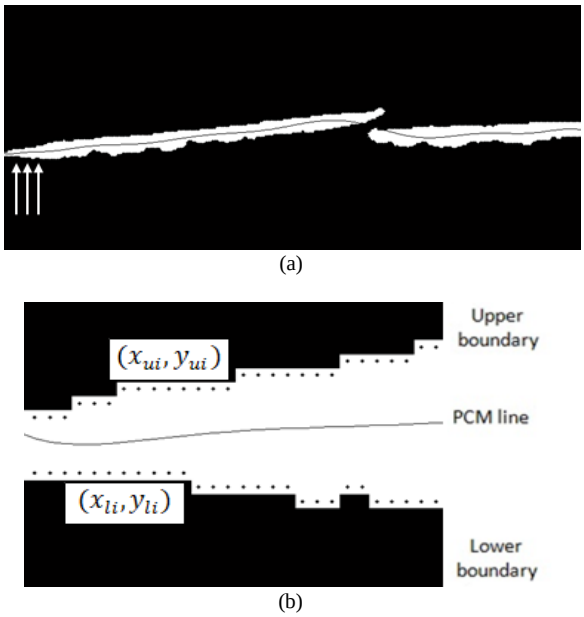

Fig. 7. (a) Upper and lower boundary of bone areas is determined by scanning upside or downside, starting from pixel (x_i, y_i) on the PCM line (b) one segment of the bone area is enlarged to show the pixels in the upper and lower boundary.

Polynomial Tangent Perpendicular Line (PTPL) method. The most important in PTPL method is to determine the straight line $g(x_i) = m_2 \, x_i + C$, which perpendicular to the tangent PCM line on the i^{th} column. The result of this method is shown in Fig. 8. Line $g(x_i)$ crosses the PCM line on (x_i, y_i), with the top pixel on the upper boundary coordinates, (x_{ui}, y_{ui}), and the bottom pixel on the lower boundary's coordinates, (x_{li}, y_{li}). To ensure $g(x_i)$ precisely perpendicular to the PCM line, we need to calculate the gradient of the tangent PCM line. Let m_1 is a gradient of the tangent PCM line on each column, and $f(x)$ is the polynomial equation of PCM line, the correlation of both will satisfy (11). If $f(x)$ is an n order polynomial equation, the gradient of the PCM line will have an $(n-1)$ degree.

$$m_1 = \frac{d}{dx} \left(\sum_{k=0}^{n} p_n x^n \right) \tag{11}$$

$$m_1 \, m_2 = -1 \tag{12}$$

Moreover, $f(x)$ and $g(x_i)$ would fulfill (12) and gradient of $g(x_i)$ in i^{th} column, m_2, could be calculated. The constant, C, of $g(x_i)$ is calculated using crossed point of $g(x_i)$ to PCM line at (x_i, y_i). Then, this quation is utilized to obtain the pixels which fulfill the $g(x_i)$ line from lower to upper boundaries.

Axis Perpendicular Line (APL) method. As a comparative method, we also proposed an APL method. In this method, a straight line $g(x_i)$ is designed to cross the PCM line at pixel (x_i, y_i) and perpendicular to the x – axis of the image area. Top end of $g(x_i)$ line ended to the upper boundary, and bottom end of the $g(x_i)$ line ended to the lower edge. The upper boundary, lower boundary and the PCM line – $g(x_i)$ crossing point have the same x coordinates. The result is shown on Fig. 9.

(a)

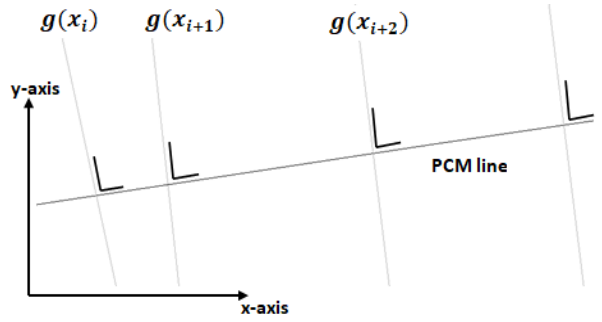

(b)

Fig. 8. (a) The straight line, $g(x_i)$, is perpendicular to the tangent line of PCM on the i^{th} column (b) one segment of the bone area is enlarged to show the $g(x_i)$ line.

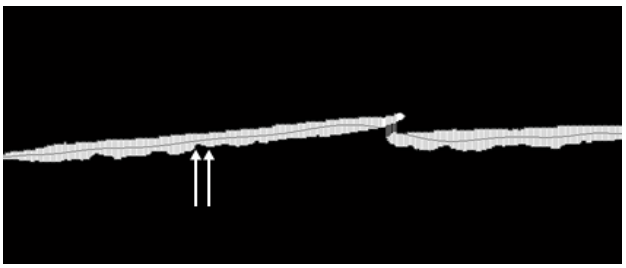

(a)

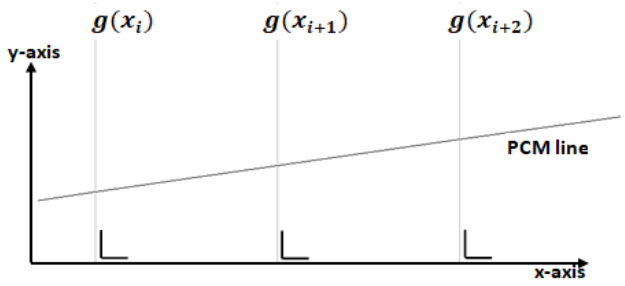

(b)

Fig. 9. (a) The $g(x_i)$ line is perpendicular to the x – axis of the bone area (b) one segment of the bone area is enlarged to show the $g(x_i)$ line.

4) Intensity gradient

The total intensity (normalized) in the i^{th} column, $J_{tot}(x_i)$, is the total of pixels intensity along $g(x_i)$ straight line at rows of $k = 1, 2, \dots, K$ in the i^{th} column, where K is the total number of rows from lowest edge to top boundary along the $g(x_i)$ line. If $J(x_{ik}, y_{ik})$ is intensity of a pixel (x_k, y_k) at the $g(x_i)$, then

$$J_{tot}(x_i) = \sum_{k=1}^{K} J(x_{ik}, y_{ik}) \tag{13}$$

The intensity gradient, $\nabla J(x_i)$, is calculated from difference of total intensity between adjacent columns. If $\alpha_{x_i} = \frac{\partial J_{tot}(x_i)}{\partial x_i}$ and $\alpha_{y_i} = \frac{\partial J_{tot}(x_i)}{\partial y_i}$ are the partial difference of total intensity in the x – axis and y – axis, then,

$$\nabla J(x_i) = [\alpha_{x_i} \quad \alpha_{y_i}] \tag{14}$$

$$|\nabla J(x_i)| = \sqrt{(\alpha_{x_i})^2 + (\alpha_{y_i})^2} \tag{15}$$

$J_{tot}(x_i)$ is affected by $g(x_i)$ meanwhile $g(x_i)$ is function of x and y. Therefore, (14) could be simplified and rewritten as (16) and (17). The value of Δx is always one, whereas the Δy is the distance between two adjacent center mass lying on the PCM line in the adjacent columns. It ensures, the Δx and Δy influenced the intensity gradient in the PTPL method. However, in the APL method, the intensity gradient is affected by the Δx only.

$$\alpha_{x_i} = \frac{J_{tot}(x_i + \Delta x) - J_{tot}(x_i)}{(x_i + \Delta x) - x_i} \tag{16}$$

$$\alpha_{y_i} = \frac{J_{tot}(x_i + \Delta x) - J_{tot}(x_i)}{(y_i + \Delta y) - y_i} \tag{17}$$

Fig. 10 shows the implementation of intensity gradient calculation using PTPL and APL methods. In the no – fracture bone, both methods produce a small intensity gradient between two adjacent column (close to zero). When the fracture occurred, at the beginning and the end of the fracture occurrence, the intensity gradient shows a significant amplitude, positive or negative higher than intensity gradient of the no – fracture bone.

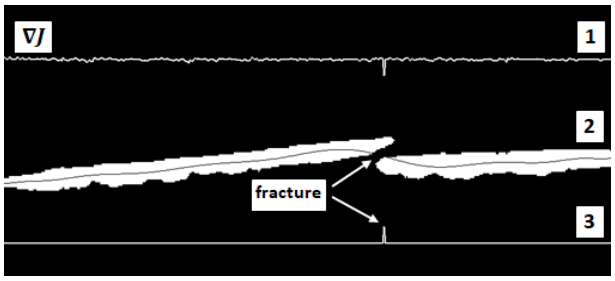

(a)

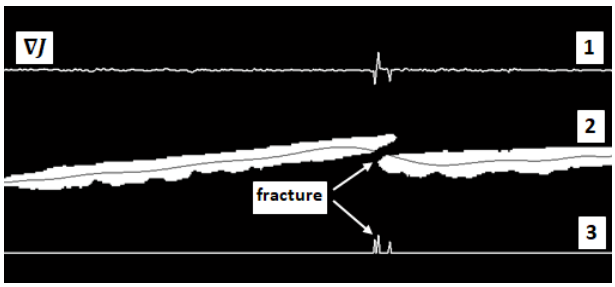

(b)

Fig. 10. Intensity gradient calculation (a) using the PTPL method and (b) using the APL method. The sequence (1 – 3) on (a) and (b) is: (1) amplitude of intensity gradient, (2) bone area with PCM line and boundary pixels, and (3) the fracture detection.

Let $\nabla J(x_i)$ and $\overline{\nabla J(x_i)}$ denote the intensity gradient in the i^{th} column and its average, M is the number of columns in the bone area, then the standard deviation, σ, is given as (18). The standard deviation of intensity gradient, σ, could be used to identify the occurrence of bone fracture.

$$\sigma = \sqrt{\frac{\sum_{i=0}^{M}\left(\nabla J(x_i) - \overline{\nabla J(x_i)}\right)^2}{M-1}} \quad (18)$$

The bone undergoes fractured in one or several locations if its standard deviation is higher than the standard deviation of the no – fracture bone, σ_b.

$$\sigma = \begin{cases} \leq \sigma_b & no-fracture \\ > \sigma_b & fracture\ \ bone \end{cases} \quad (19)$$

Applying this concept to the US bone image, the fractured bone is detected as shown in Fig. 10. And the location of the higher intensity gradient than the threshold value indicate the location of the fracture. The both PTPL and APL methods could identify fractured at the same location even though they result in a different accuracy and pattern.

III. Experimental Results

A. Calibration using no – fracture bone

A piece of no – fracture femoral bovine bone is used as a reference for determining fracture of other tested femoral bone. The image produced by the scanning process where the probe is in the transverse position is shown in Fig. 11(a.2). The image is in curved contour. The 10^{th} order polynomial is implemented to obtain the mass center of the bone area, which the PCM line has a minimum error to the average mass center of each column in the bone area. Both PTPL and APL methods give the nearly same intensity gradient amplitude across all columns, proving that the bone is really in a state not cracked.

Nevertheless, the US scanning with parallel probe position produced a flat contour image, as shown in Fig. 11(b.2). The 7^{th} order polynomial is used to fit the mass center each column to the PCM line. Implementation of PTPL and APL methods to this image produce the same value of the intensity gradient.

According to the Table I, the mean, maximum and standard deviation of the no – fracture femoral bone produced by APL method is higher than the values produced by PTPL. This fact shows that PTPL has higher sensitivity in the detecting fracture than APL method. For the parallel probe position, the results are relatively similar between the PTPL and APL methods, because the resulting 2D image has a nearly flat contour from end to end. The maximum intensity gradient and the standard deviation are used as the threshold value of bone surface fracture detection. Let σ_{curv} and σ_{flat} are the standard deviation for femoral bovine bone image, then

$$\sigma_{curv} = \begin{cases} \leq 0.354 & no-fracture \\ > 0.354 & fracture\ \ bone \end{cases} \quad (20)$$

$$\sigma_{flat} = \begin{cases} \leq 0.337 & no-fracture \\ > 0.337 & fracture\ \ bone \end{cases} \quad (21)$$

To detect fracture location, we use the maximum intensity gradient, $|\gamma(x,y)_{curv}|$ and $|\gamma(x,y)_{flat}|$ as given by (22) and (23) for curved and flat contour.

$$|\gamma(x,y)_{curv}| = \begin{cases} \leq 1.71 & no-fracture \\ > 1.71 & fracture\ \ bone \end{cases} \quad (22)$$

$$|\gamma(x,y)_{flat}| = \begin{cases} \leq 1.42 & no-fracture \\ > 1.42 & fracture\ \ bone \end{cases} \quad (23)$$

The standard deviation on (20) – (21) and maximum value of intensity gradient on (22) – (23) are used to determine the fracture and its location in the other femoral tested bones.

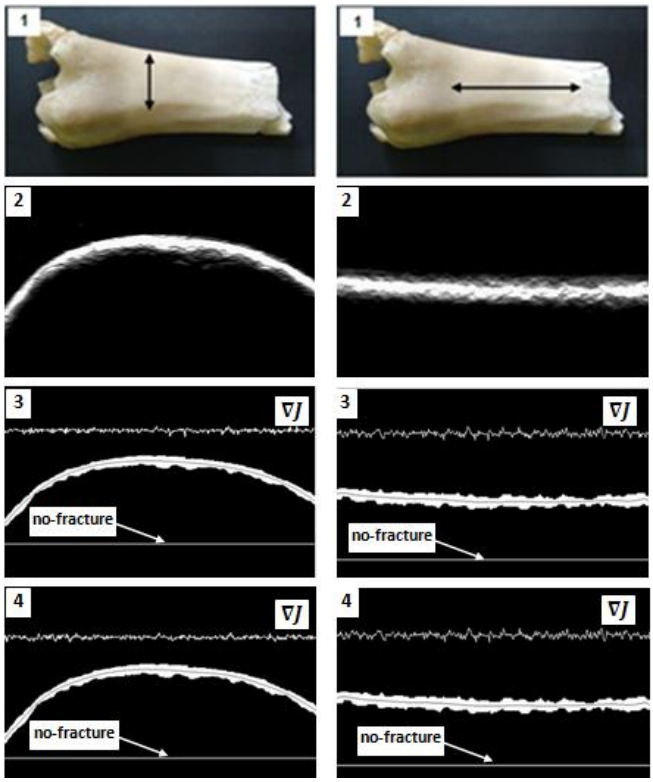

(a) (b)

Fig. 11. Fracture detection of the no – fracture femoral bone, with probe position to the bone length (a) on transverse position and (b) on parallel position. The row sequences from (1) to (4) are: (1) bone and probe position, (2) 2D B – mode US image, (3) fracture detection using PTPL method, (4) fracture detection using APL method.

TABLE I
Intensity Gradient of No – Fracture Femoral Bone Image

Probe Position	Method	Intensity gradient (normalized)		
		Max	Mean	Std Dev.
Transverse	PTPL	1.69	0.35	0.35
	APL	1.73	0.4	0.36
	Average	1.71	0.38	0.35
Parallel	PTPL	1.42	0.34	0.34
	APL	1.42	0.34	0.34
	Average	1.42	0.34	0.34

B) Oblique – fracture femoral bone

The image for transverse probe position is shown in Fig. 12(a) and for lateral/parallel probe position is shown in Fig. 12(b). The PTPL and APL method of both probe position detect fractures in the same position. For a transverse probe position, the 2D image is in the curved contour, while for a parallel probe position, the B – mode image is in the flat contour.

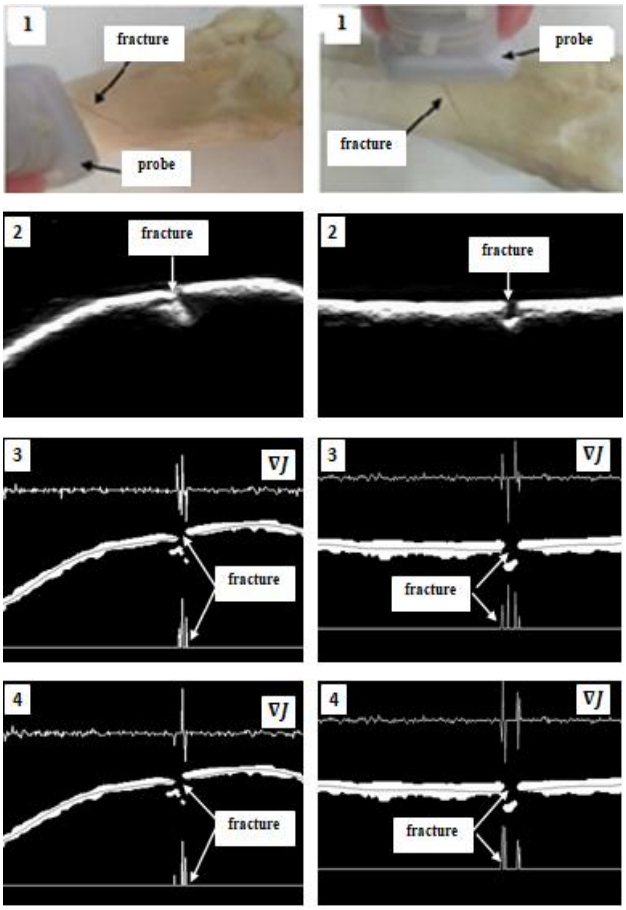

(a) (b)

Fig. 12. Bone fracture detection on an oblique pattern, with probe position to the bone length (a) on transverse position (b) on parallel position. The row sequences from (1) to (4) are: (1) bone and probe position, (2) B – mode US image, (3) fracture detection using PTPL method (4) fracture detection using APL method.

For curved contour image, the PCM line is determined using the 12th order polynomial and the fracture detection uses the formula of (20) and (22). Whereas for parallel probe position, the 2D B – mode image is in the flat contour. We obtain the best PCM line using the 8th order polynomial. And the fracture is detected using the rule of (21) and (23).

TABLE II
INTENSITY GRADIENT OF OBLIQUE – FRACTURE FEMORAL BONE IMAGE

Probe Position	Method	Intensity gradient (normalized)		
		Max	Mean	Std Dev.
Transverse	PTPL	15.84	0.51	1.33
	APL	15.84	0.49	1.146
Parallel	PTPL	10.97	0.28	0.844
	APL	10.83	0.32	1.023

Table II confirms Fig. 12.a (3 – 4) and Fig. 12.b (3 – 4), that the proposed method has success to detect a fracture of a femur bone on one or several positions of its surface. The standard deviation is greater than the standard deviation on (20) and (21), thus fulfilling the criteria that the bone tested is broken.

C) Fracture on other bone type

The following are the results of the PTPL and APL fracture detection method implementation on bovine long bone such as the tibia, metatarsal, humerus, ulna, radius, metacarpal, phalange, and costa with transverse, oblique and comminuted fracture types, as shown in Fig. 13. For comminuted type, fractures are detected in several adjacent locations, with varying fracture width. Determination of standard deviation, σ, and maximum intensity gradient, $\gamma(x, y)$, as a reference to detect fracture and its position is done by initial scanning at the location of no – fracture of each bone type. Fig. 13 confirms that the proposed method has succeeded in detecting the presence of fracture and their positions for various types of bovine bone.

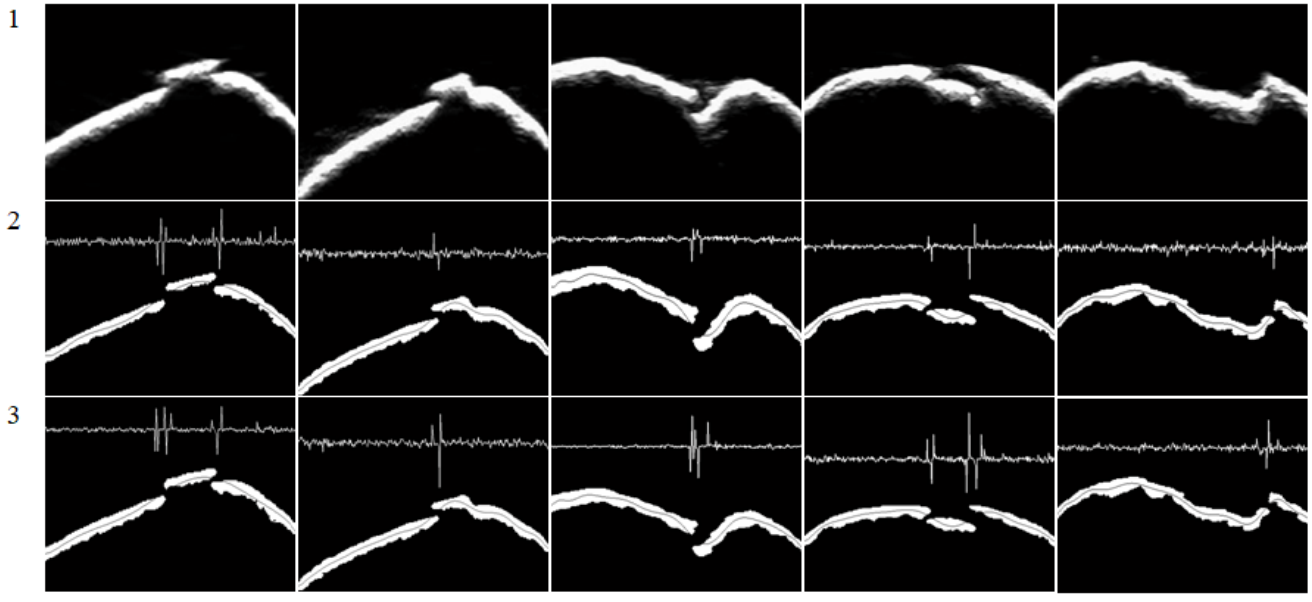

(a) (b) (c) (d) (e)

Fig. 13. Fracture detection in some bovine bone samples. Row sequences from 1 to 3 are: 1) 2D B–mode image 2) fracture detection using PTPL method, and 3) fracture detection using APL method. While the column sequences from (a) to (e) are: (a) costa on comminuted fracture (b) costa on oblique fracture (c) tibia on oblique fracture (d) ulna on comminuted fracture (e) metatarsal on comminuted fracture.

IV. Discussion

Several studies of bone fracture have succeeded in separating the bone area from surrounding soft tissue, found the outer bone contour and detected the fracture happened. Hacihaliloglu et al. have presented a method for bone segmentation from ultrasound images using intensity – invariant local image phase and detected the fracture. Their research produced a 41% improvement in surface localization error over the previous 2D phase symmetry method with a localization accuracy of 0.6 mm and mean errors in estimating fracture displacements below 0.6 mm [31]. Demers et al. detected the induced long bone fractures from cadaver model. Their research result the sensitivity/specificity of fracture detection with range 87.3 – 95.2 / 69.8 – 88.9% for proximal tibia, distal radius and temporal bone types [36].

In this paper, we have proposed method to detect bone fracture accurately based on high order polynomial equation and intensity gradient calculation of the 2D – bovine bone US – images. This proposed method offered another alternative using a simple basic equation, therefore, the processing time could be shortened and the decisions could be obtained quickly and accurately. Our proposed method proved that the use of the high – order polynomial approaches combined with PTPL and APL methods produced 100% accuracy in determining the presence of transverse, oblique and comminuted fractures on the many type bovine long bones.

A. *Effect of polynomial order*

Polynomial equations are used to anticipate uncertain surface contour characteristics. High – order polynomial could follow changing pattern flexibly to obtain the precise position of the center of mass. The use of an improper polynomial order causes an error in the definition of column, $g(x_i)$, and result in fracture detection errors. The polynomial orders for various bone types and various fractures are shown in Fig. 14. No – fracture bone has the lowest polynomial order. If there is a fracture, the polynomial order will increase. The more fractures location detected cause the increment of polynomial order, and the polynomial order on the curved contour is higher than the flat contour.

B. *Width fracture evaluation*

In our previous research, we have proposed the estimation of wire phantom position using the polynomial approach on 2D - US images [35]. The research resulted that the distance of 1-centimeter between two wire phantoms is equal to 122.72 pixels. We implemented these result for evaluating the fracture width. Table III and Table IV present the fracture width evaluation of curved and flat contour surface of tested bones. The accuracy of detection on start – end fracture position affects the fracture width estimation.

The PTPL method is more accurate than APL method. In the curved contour bone surface, the estimation width fracture using PTPL method has 1.14% error with the mean absolute error (MAE) of 0.016 mm. While the APL method has 2.63% error with the MAE of 0.04 mm (see Table III). Meanwhile, in the flat contour bone surface, the estimation width fracture using PTPL method has 2.41% error with the MAE of 0.03 mm while the APL method has 3.21% error with the MAE of 0.04 mm (see Table IV).

C. *Pattern evaluation*

The higher intensity gradient than the threshold value identifies the start of the fracture area. In the fractures area, the total intensity of each column has almost the same value, and its gradient approaches zero (or below the threshold value). And, at the end of the fracture, the intensity gradient will exceed the threshold value with the gradient direction opposite from the gradient direction at the beginning of the fracture.

The PTPL method and the APL method produce different fracture pattern on the fracture detection of the same bone. Fig. 15 shows the comparison of fracture pattern between PTPL and APL methods on curved contour, according to Fig. 12(a) on sequence (3 – 4). Fracture detection using the PTPL method was marked as 1 – 2, whereas using the APL method, the fracture was marked as 3 – 4.

Fig. 16 shows the comparison of fracture pattern between PTPL and APL methods on flat contour surface, according to Fig. 12(b) on sequence (3 – 4). A fracture was marked by 1 until 5 using the PTPL method and 6 until 11 using the APL method. Number 3 – 4 and 8 – 9 are decided as a fracture position because there is a change of gradient direction.

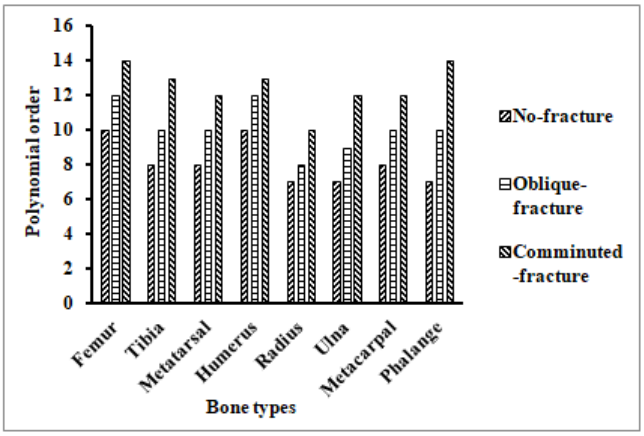

(a)

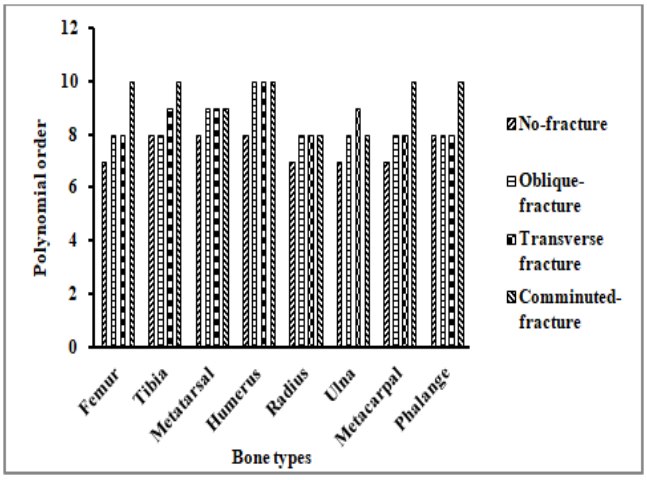

(b)

Fig. 14. Comparison of polynomial order on various type fractured bovine bones for: (a) curved contour bone surface (b) flat contour bone surface.

TABLE III
WIDTH FRACTURE ESTIMATION OF CURVED CONTOUR BONE SURFACE

Bone sample	Method	Intensity gradient (norm)		Width Measurement (mm)		Error (%)
		Std. Dev.	Max	Manual	Propose Method	
1	PTPL	0.498	8.752	1.4	1.39	0.71
	APL	0.533	9.219		1.47	5
2	PTPL	0.664	6.686	1.4	1.39	0.71
	APL	0.689	8.294		1.47	5
3	PTPL	0.463	3.229	1.4	1.47	5
	APL	0.477	3.865		1.47	5
4	PTPL	1.304	6.545	1.4	1.39	0.71
	APL	1.363	6.545		1.55	10.7
5	PTPL	0.641	4.957	1.4	1.39	0.71
	APL	0.703	6.922		1.47	5
6	PTPL	0.972	3.261	1.4	1.47	5
	APL	1.383	3.422		1.55	10.7
7	PTPL	2.062	1.925	1.4	1.47	5
	APL	2.338	2.027		1.47	5
8	PTPL	0.585	4.15	1.4	1.47	5
	APL	0.614	4.472		1.55	10.7

Note: Bone samples are: 1. Femur, 2. Tibia, 3. Metatarsal, 4. Humerus, 5. Radius, 6. Ulna, 7. Metacarpal, and 8. Phalange.

TABLE IV
WIDTH FRACTURE ESTIMATION OF FLAT CONTOUR BONE SURFACE

Bone sample	Method	Intensity gradient (norm)		Width Measurement (mm)		Error (%)
		Std. Dev.	Max	Manual	Propose Method	
1	PTPL	0.438	10.376	1	1.06	6
	APL	0.467	10.376		1.06	6
2	PTPL	0.498	14.269	1.4	1.39	0.71
	APL	0.527	14.296		1.39	0.71
3	PTPL	0.455	6.69	1	0.98	2
	APL	0.463	6.688		0.98	2
4	PTPL	0.49	12.265	1	1.06	6
	APL	0.498	12.265		1.06	6
5	PTPL	1.168	14.735	1.4	1.39	0.71
	APL	1.201	15.26		1.47	5
6	PTPL	0.855	8.229	1	1.06	6
	APL	0.902	8.751		1.06	6
7	PTPL	0.449	8.925	1	1.06	6
	APL	0.467	9.139		1.06	6
8	PTPL	0.874	10.569	1.4	1.47	5
	APL	0.883	10.583		1.47	5

Bone samples are: 1. Femur on transverse fracture, 2. Tibia on oblique fracture, 3. Metatarsal on transverse fracture, 4. Humerus on transverse fracture, 5. Radius on oblique fracture, 6. Ulna on transverse fracture, 7. Metacarpal on transverse fracture, 8. Phalange on oblique fracture.

V. CONCLUSION

From the above discussion, we concluded that the high order polynomial approach as the base of the intensity gradient calculation to detect the occurrence and estimate the width of bone fracture worked accurately. PTPL and APL methods deliver 100% accuracy in the detection of bone fracture occurrence.

Detection of fracture width by PTPL method in curved contour is more accurate than using APL method. For 1 – mm artificial bovine bone fracture, the PTPL method produce MAE of 0.016 mm while the APL method has MAE of 0.04 mm. For fracture width estimation on flat contour, the PTPL method gave MAE of 0.03 mm and the APL method produce MAE of 0.04 mm. It can be concluded that the PTPL method which considers the direction of the gradient between two adjacent mass centers results in the more accurate measurement of fracture width than the APL method, for all tested bone types.

For future work, it is necessary to improve the US image calibration method, so that the scale of the scalar to the pixel of 2D – US image is smaller and the accuracy of the fracture width detection could be improved. And then applying its

method to other bone types and the human bone with the real fracture.

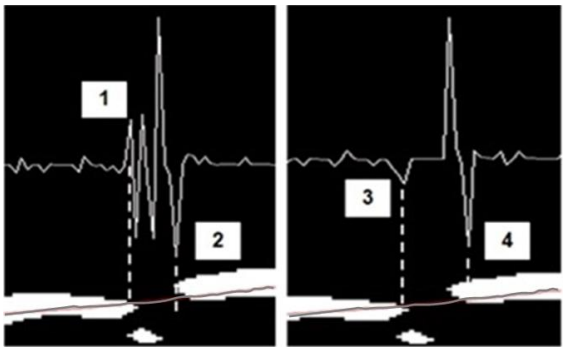

(a) (b)

Fig. 15. Pattern of oblique femur fracture on curved contour using (a) PTPL method and (b) APL method.

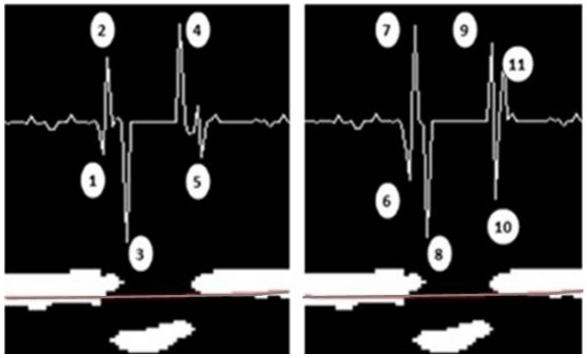

(a) (b)

Fig. 16. Pattern of oblique femur fracture on flat contour using (a) PTPL method and (b) APL method.

REFERENCES

[1] A. Oryan, S. Monazzah, and A. Bigham-Sadegh, "Bone Injury and Fracture Healing Biology," *Biomed Environ Sci*, vol. 28, no. 1, pp. 57–71, 2015.

[2] John A Dent, "Fractures Long Bones - Upper Limb (includes hand)," *Ninewells Hosp. and Med. School*, Dundee, September 2008.

[3] M. G. Abrahamyan, "On the Physics of the Bone Fracture," *Int J Orthopaedics and Traumatology*, vol. 2, no. 1, pp. 1–4, 2017.

[4] J. F. Keating, A. H. R. W. Simpson, and C. M. Robinson, "The management of fractures with bone loss," *J Bone and Joint Surgery*, vol. 87, pp. 142–150, 2005.

[5] H. K. Uhthoff, P. Poitras, and David S. Backman, "Internal plate fixation of fractures : short history and recent developments," *J Orthopaedic Science*, vol. 11, no. 2, pp. 118–126, 2006.

[6] D. I. Rowley, *War wounds with fractures: a guide to surgical management*. Geneva: Int. Committee of the Red Cross, 1996.

[7] T. Takahashi, Y. Ohara, and M. Yamada, "Improving X-ray Image Quality based on Human-Body Thickness and Structure Recognition," *Fujifilm Res Dev*, vol. 62, pp. 30–37, 2016.

[8] D. W. Yap, Y. Chen, W. K. Leow, T. Sen Howe, and M. A. Ping, "Detecting Femur Fractures by Texture Analysis of Trabeculae," in *Proc.17th Int. Conf. on Pattern Recognition*, 2004, pp. 2–5.

[9] J. Liang, B. Pan, Y. Huang, and X. Fan, "Fracture Identification of X-Ray Image," in *Proc. Int. Conf. on Wavelet Analysis and Pattern Recognition*, 2010, pp. 11–14.

[10] C. Roll, J. Schirmbeck, F. Muller, C. Neumann, and B. Kinner, "Value of 3D Reconstructions of CT Scans for Calcaneal Fracture Assessment," *American Orthopaedic Foot and Ankle Society*, vol. 37, no. 1, pp. 1211–1217, 2016.

[11] J. Wu, A. Belle, C. H. Cockrell, K. R. Ward, and R. S. Hobson, "Fracture detection and quantitative measure of displacement in pelvic CT images," in *IEEE Int. Conf. on Bioinformatics and Biomedicine Workshops*, 2011, pp. 600–606.

[12] J. Sabol, R. Ralbovska, and J. Hudzietzova, "Important role of radiation protection in specific applications of X-rays and radionuclides in bioengineering," in *The 4th IEEE Int. Conf. on E-Health and Bioengineering-EHB*, 2013, pp. 4–7.

[13] K. Eckert, O. Ackermann, and B. Schweiger, "Ultrasound evaluation of elbow fractures in children," *J of Medical Ultrasonics*, vol. 40, pp. 443–451, 2013.

[14] H. Matsuki and J. Shibano, "Elastic modulus of the femoral trochanteric region measured by scanning acoustic microscopy in elderly women," *J of Medical Ultrasonics*, vol. 42, pp. 303–313, 2015.

[15] K. Eckert, O. Ackermann, and N. Janssen, "Accuracy of the sonographic fat pad sign for primary screening of pediatric elbow fractures : a preliminary study," *J of Medical Ultrasonics*, vol. 41, pp. 473–480, 2014.

[16] N. E. Jacob and M. Wyawahare, "Survey of Bone Fracture Detection Techniques," *Int J Computer Application*, vol. 71, no. 17, pp. 31–34, 2013.

[17] R. Rokhana and S. Anggraini, "Using Of Array Of 8 Ultrasonic Transducers On Accoustic Tomography for Image Reconstruction," in *Proc. Int. Electronics Symposium (IES)*, 2015, pp. 20–25.

[18] R. A. Sofferman, "Physics and Principles of Ultrasound," in *Ultrasound of the Thyroid and Parathyroid Glands*, A. T. Ahuja, Ed. Springer Science and Business Media, 2012, pp. 9–20.

[19] S. W. Hughes, "Medical ultrasound imaging," *Physics Education*, vol. 36, no. 6, pp. 468–475, 2001.

[20] R. Rokhana and S. Anggraini, "Classification of Biomedical Data of Thermoacoustic Tomography to Detect Physiological Abnormalities in the Body Tissues," in *Int. Electronics Symposium (IES)*, 2016, pp. 60–65.

[21] J. J. Kaufman, G. Luo, and R. S. Siffert, "Ultrasound Simulation in Bone," *IEEE Trans. on Ultrasonics, Ferroelectrics, and Frequency Control*, vol. 55, no. 6, pp. 1205–1218, 2007.

[22] P. Moilanen, "Ultrasonic Guided Waves in Bone," *IEEE Trans. on Ultrasonics, Ferroelectrics, and Frequency Control*, vol. 55, no. 6, pp. 1277–1285, 2008.

[23] K. M. Meiburger, U. R. Acharya, and F. Molinari, "Automated localization and segmentation techniques for B-mode ultrasound images : A review," *Computer in Biology and Medicine*, vol. 92, pp. 210–235, 2018.

[24] D. Shao, T. Zhou, F. Liu, S. Yi, Y. Xiang, L. Ma, X. Xiong, and J. He, "Ultrasound speckle reduction based on fractional order differentiation," *J of Medical Ultrasonics*, vol. 44, no. 3, pp. 227–237, 2017.

[25] J. R. J and M. S. Chithra, "Bayesian denoising of ultrasound images using heavy-tailed Levy distribution," *IET Image Processing*, vol. 9, no. 4, pp. 338–345, 2015.

[26] M. Rafati, M. Arabfard, M. Rafati, R. Zadeh, and M. Maghsoudloo, "Assessment of noise reduction in ultrasound images of common carotid and brachial arteries," *IET Computer Vision*, vol. 10, no. 1, pp. 1–8, 2016.

[27] S. Rueda, C. L. Knight, A. T. Papageorghiou, and J. A. Noble, "Feature-based fuzzy connectedness segmentation of ultrasound images with an object completion step," *Medical Image Analysis*, vol. 26, no. 1, pp. 30–46, 2015.

[28] D. Gupta, R. S. Anand, and B. Tyagi, "Despeckling of ultrasound images of bone fracture using M-band ridgelet transform," *Optik*, vol. 125, no. 3, pp. 1417–1422, 2014.

[29] T. Karlita, E. M. Yuniarno, I. K. E. Purnama, and M. H. Purnomo, "Automatic Bone Outer Contour Extraction from B-Modes Ultrasound Images Based on Local Phase Symmetry and Quadratic Polynomial Fitting," in *Second Int. Workshop on Pattern Recognition-SPIE*, 2017, vol. 10443, pp. 1–6.

[30] P. Kovesi, "Symmetry and Asymmetry from Local Phase," in *Tenth Australian Joint Converence on Artificial Intelligence*, 1997.

[31] I. Hacihaliloglu, R. Abugharbieh, Antony J. Hodgson, R. N. Rohling, and P. Guy, "Automatic bone localization and fracture detection from volumetric ultrasound images using 3-D local phase features," *Ultrasound in Medicine and Biology*, vol. 38, no. 1, pp. 128–144, 2012.

[32] R. Jia, S. J. Mellon, S. Hansjee, A. P. Monk, D. W. Murray, and J. A. Noble, "Automatic Bone Segmentation in Ultrasound Images Using Local Phase Features and Dynamic Programming," in *Int. Symposium on Biomedical Imaging*, 2016, pp. 1005–1008.

[33] M. Talibi-Alaoui and A. Sbihi, "Application of a Mathematical Morphological Process and Neural Network for Unsupervised Texture Image Classification with Fractal Features," *IAENG International Journal of Computer Science*, vol. 39, no. 3, pp. 286–294, 2012.

[34] A. Sopharak, B. Uyyanonvara, and S. Barman, "Automatic Microaneurysm Detection from Non-dilated Diabetic Retinopathy Retinal Images Using Mathematical Morphology Methods," *IAENG International Journal of Computer Science*, vol. 38, no. 3, pp. 295–301, 2011.

[35] R. Rokhana, E. M. Yuniarno, I. K. E. Purnama, and M. H. Purnomo, "Estimation of wire phantom's position in ultrasound probe

calibration based on polynomial equation," in *Int. Conf. on Intelligent Systems, Metaheuristics & Swarm Intelligence*, 2017, no. 1, pp. 137–141.

[36] G. Demers, S. Migliore, D. R. Bennett, M. D. Mccann, C. J. Kalynych, K. Falgatter, and L. Simon, "Ultrasound Evaluation of Cranial and Long Bone Fractures in a Cadaver Model," *Military Medicine*, vol. 177, no. 7, pp. 836–839, 2012.

Rika Rokhana is currently a Ph.D student since 2016 at the Electrical Engineering Department, Institut Teknologi Sepuluh Nopember, Surabaya, Indonesia.
She also has been with Politeknik Elektronika Negeri Surabaya, Indonesia since 1998. Her research interest including Medical Image Processing and Computer Vision. She is an IAENG Member.

Eko Mulyanto Yuniarno received the bachelor degree in 1994, Master of Technology in 2004 and Ph.D degree in 2013 from Electrical Engineering Department, Institut Teknologi Sepuluh Nopember, Surabaya, Indonesia. Currently, he is a staff of Computer Engineering Department, Institut Teknologi Sepuluh Nopember, Surabaya, Indonesia.
His research interest is in Image Processing, Computer Vision and 3D – Reconstruction

I Ketut Eddy Purnama received the bachelor degree in Electrical Engineering from Institut Teknologi Sepuluh Nopember, Surabaya, Indonesia in 1994. He received his Master of Technology from Institut Teknologi Bandung, Indonesia in 1999. And, he received Ph.D degree from University of Groningen, the Netherlands in 2007. Currently, he is a staff of Computer Engineering Department, Institut Teknologi Sepuluh Nopember, Surabaya, Indonesia.
His research interest is in Data Mining, Medical Image Processing and Intelligent System.

Kayo Yoshimoto received the B.E and M.E. degrees in mechanical engineering from Osaka University in 2009 and 2011, respectively. She completed the doctoral program at Osaka University (Graduate School of Medicine) in 2014. She became a research associate of the Dept. of Electrical and Information Engineering of Osaka City University since 2014. Her current research interests include Medical Engineering and Nursing Engineering.

Hideya Takahashi received his BE, ME and Ph.D in electrical engineering from Osaka City University in 1982, 1984, and 1992, respectively. Since 1987, he is a faculty member at Osaka City University. And, he has been a Professor of the Dept. of Electrical and Information Engineering, Osaka City University since 2011. His current research interest include interactive 3D display, retinal projection display, and wearable computers. He is a member of SPIE and OSA.

Mauridhi Hery Purnomo earned his bachelor degree from Institut Teknologi Sepuluh Nopember, Surabaya, Indonesia, in 1985 then his Master of Engineering and Ph.D degrees from Osaka City University, Osaka, Japan in 1995 and 1997 respectively. He joined ITS in 1985 and has been a Professor since 2004. His current interest include intelligent system applications on electric power system, control and medical signal processing. He is an IAENG and IEEE Member.